Draft: Multipoint Shape Optimisation of an Automotive Radial Compressor Using a Coupled Computational Fluid Dynamics and Genetic Algorithm Approach

Stefan Tüchler[a,*], Zhihang Chen[a], and Colin D. Copeland[a]

[a]*Powertrain and Vehicle Research Centre, Department of Mechanical Engineering, University of Bath, Claverton Down, Bath BA2 7AY, United Kingdom*

Abstract

Automotive turbochargers operate over a wide range and require high efficiencies and pressure ratios. These conflicting requirements and a myriad of design parameters render iterative design techniques unfeasible. However, over the last decades the combination of numerical flow solvers and evolutionary algorithms has established itself as a viable option in the pursuit of reaching desired performance characteristics.

This study seeks to perform a three-dimensional, multipoint and multiobjective optimisation of an automotive radial compressor by modifying blade shape as well as the meridional contour of the flow path. The method couples steady-state computational fluid dynamics (CFD) with a genetic algorithm (GA) to maximise isentropic efficiency in the region close to surge, while ensuring no significant reduction in choke margin.

The results of two optimisation studies are presented and a flow-field analysis based on entropy generation rate is carried out revealing regions of flow improvement. The results are further compared against experimental data, indicating good agreement between the numerical and test data. The experiments however imply a detrimental impact on the surge margin for larger impeller speeds, which is attributed to unfavourable blade loading. Two additional optimisation runs are presented mitigating the effect of loading unbalance between main blade and splitter.

Keywords: Optimisation, Genetic Algorithm, Radial Turbomachinery, Computational Fluid Dynamics, Entropy Generation, Blade Loading

*Corresponding author

Email address: S.Tuechler@bath.ac.uk (Stefan Tüchler)

Nomenclature

c_p Specific heat capacity at const. pressure [J/kg-K]

y^+ Dimensionless wall distance [-]

A Area

P Penalty function

R Specific gas constant [J/kg-K]

T Static temperature [K]

Π Pressure ratio [-]

$\dot{S}$ Entropy generation rate [W/m^3-K]

$\dot{m}$ Mass flow rate [kg/s]

η Efficiency [-]

h Specific enthalpy [J/kg]

k Turbulent kinetic energy [J/kg]

p Pressure [Pa]

r Mesh refinement factor [-]

s Specific entropy [J/kg-K], Dimensionless streamwise coordinate [-]

w Weighting factor

ω Spec. turb. dissipation rate [1/s]

ANN Artificial neural network

BL Baseline

CFD Computational fluid dynamics

DoE Design of experiments

GA Genetic algorithm

GCI Grid convergence index

ICE Internal combustion engine

is Isentropic

lb Lower boundary

LE Leading edge

LU Loading unbalance

MB Main blade

MP Mach peak

NL Negative loading

NN Neural network

OF Objective function

OP Operating point

pp Percentage points

ps Pressure surface

RANS Reynolds-averaged Navier-Stokes

RDE Real driving emissions

RMS Root mean squared

SP Splitter, single passage

SS Suction surface

SST Shear stress transport

TT Total-to-total

up Upper boundary

X Design variable

1. Introduction

Radial compressors excel at providing large pressure ratios over a wide operating range and have become a widespread application in various engineering disciplines. One of these disciplines is the automotive industry, which has moved into the focus of attention as a consequence of increasing awareness of the ecological footprint of road transport and customer awareness to fuel economy and costs. In combination with the depletion of fossil fuel resources as well as increasingly stringent emission regulations this forced manufacturers to modify the traditional powertrain development resulting in a increasing drivetrain electrification as well as internal combustion engine (ICE) downsizing. Downsizing in combination with a turbo- or supercharger is now an established technology ensuring lower fuel consumption and pollutant emissions and continues to be of great interest as stricter requirements regarding Real Driving Emissions (RDE) are introduced.

Radial compressors are complex geometries resulting in an intricate, three-dimensional flow field. Analytical relations often fall short of providing sufficient insight and advent of reliable and accurate numerical modeling techniques, such as computational fluid dynamics (CFD), has allowed to study the complex fluid dynamics within turbomachinery components with ever greater accuracy and detail[1, 2, 3, 4, 5, 6, 7, 8, 9].

CFD has also accelerated the design cycle of turbomachinery, shown by Sanz et al. [10], Sun et al. [11] Ping et al. [12] and Hazby et al. [13]. Nonetheless, the caveat lies in the fact that compressor design involves dealing with conflicting objectives and is inherently multi-objective, multi-point and multi-disciplinary. The aim is to generate a design that operates at high efficiency and pressure ratio, while being lightweight, compact, low cost and offering a long service life. This renders iterative design techniques resource intense and the eventual result often in need of further improvement. As a result, one is faced with the need for automatised routines.

Against this background, optimisation techniques search the best geometry to comply with a particular performance criterion. The performance criterion is formulated as an objective, fitness or penalty function that depends on a combination of input parameters subject to a set of constraints. The optimisation routine then determines a global minimum. Unfortunately, objective functions describing turbomachinery performance are rarely simple surfaces with a single extremum, but feature multiple local extrema. A large number of research efforts have been introduced to tackle this problem. They predominately resort to stochastic methods, such as evolutionary algorithms, rather than gradient-based methods. While the former are computationally more expensive, they incur a lower probability of getting trapped in a local minimum [14].

To mitigate computational expense, several research studies resorted to approx-

imate or surrogate models for compressor optimisation. While most studies neglect the influence of the volute, Ha and Kang [15], used a one-dimensional model, introduced by Japikse [16], to include its effects while minimising computational time. The study also used a Kriging method for optimisation dealing with three design parameters and showed a 1.0 % error between CFD results and optimal design through the Kriging method.

A number of studies were dedicated to combining genetic algorithms with neural networks (NN) in an effort to reduce computational workload, such as done by Cho et al. [17] and Bo and Gu [18]. Verstrate et al. [19] embarked on a multi-objective optimisation taking both finite element analysis (FEA) and fluid dynamics (CFD) into account. One of the findings of the research was that blade root thickness can mitigate structural stress penalty without detrimentally affecting aerodynamic performance. In the analysis of Kim et al. [20], a vaneless compressor geometry was parameterised using four design variables that define flow path and blade shape. The design space was established using a DoE appraoch, which was subsequently optimised using a GA in combination with a Radial Basis Neural Network (RBNN). A Pareto optimal solution indicated the trade-off relationship between efficiency and pressure ratio and demonstrated an optimisation potential ranging from 0.65 to 0.19 per cent for efficiency and 0.86 to 1.40 per cent for total pressure ratio.

The mentioned studies confined their study to the numerical domain. There are few studies in the open literature that do not exclusively validate their initial model against experimental data, but also test the optimised design.

Kim et al. [20] optimised a vaned radial compressor using the response surface method. The optimisation first focused on the impeller geometry before the vaned diffuser was optimised for a single operating point. Experimental testing of the optimised geometry at a lower rotational speed than considered in the optimisation study showed good overall agreement between CFD and the experimental data as far as the pressure ratio is concerned, but indicated a reduced choke margin and no change in the peak pressure ratio. Ibaraki et al. [21] performed multiobjective optimisation of an impeller based on a GA and an ANN. Two designs were created, with both designs aimed at providing higher peak efficiency and operating range. Experimental tests of the two designs revealed that the first design achieved a peak efficiency that is higher by 0.5 per cent, while the second design showed a decrease in peak efficiency of about 1 per cent. The recent study carried out by Oka et al [22] combined a two-dimensional inverse design method and a GA optimisation routine aiming at maximising adiabatic efficiency and pressure ratio. The resulting optimised geometry promised a 2 % efficiency gain and a 5% gain in pressure ratio. Running the optimised geometry on a test bench and considering a single speedline

showed that while adiabatic efficiency remains more or less the same with a slight shift of peak efficiency towards lower mass flow rates, an increase in pressure ratio is witnessed. Considerable work on compressor optimisation has been done on the transonic radial compressor developed by DLR [23, 24, 25, 26, 27]. In the study by Elfert et al. [24] an optimisation based on the evolutionary algorithm based optimization process outlined by Siller et al. [25] of a radial compressor geometry is presented. The optimised geometry indicated an increase in choke margin and a 2 % gain in efficiency. The optimised design was experimentally tested and exhibited a 1.5 % increase in isentropic efficiency and an increase in choke margin by 4.4%. However, the optimised geometry indicates a less stable behaviour at near stall conditions. The bulk of the literature on compressor optimisation focuses on single operating point optimisation and comparably little amount of attention is drawn towards multiple operating points [28, 29, 27]. Li et al. [28] as well as He and Zheng [29] aimed at addressing this gap by performing a multiobjective and multipoint optimisation. The first study [28] combined 3D-CFD, GA and a data mining procedure. The procedure proves resource intense, claiming around 1400 CPU hours for one shape optimisation. The outcome of the study resulted in 1.9 % increase in efficiency and a considerable increase in both surge and choke margin. However, while the baseline model was experimentally validated, no experimental testing was conducted confirming the findings of the optimisation study. The second study [29] employed a combined GA-ANN approach to optimise across a single speedline. Surge was determined via a convergence criterion revealing large discrepancies between the baseline model results and experiments. The optimisation resulted in an increase in peak efficiency of 2.2 % and an increase in choke margin by more than 8 %. Further optimisation studies on camber shapes were conducted resulting in further efficiency improvements. The final optimised geometry was not tested experimentally against the baseline model. Hehn et al. [27] also used a combined GA-ANN method to optimise the DLR baseline compressor on three different operating points using a total number of 45 different parameters. The optimisation achieved an increase in the total to static efficiency of 1.4% through a reduction of mixing losses within the diffuser. Although no testing of the optimised geometry was mentioned in the paper, the analysis hinted towards a considerable increase in choke margin, while surge margin seemed to be only marginally shifted towards higher mass flow rates.

There is a need for further research on both multipoint optimisation across a map and for a validation of the numerical results through experiments. Due to the inherent shortcomings of steady state CFD pertaining to unsteady effects, such as surge, experimental testing enables a direct and reliable comparison between baseline and optimised designs. Therefore the objective of this study is to introduce a mul-

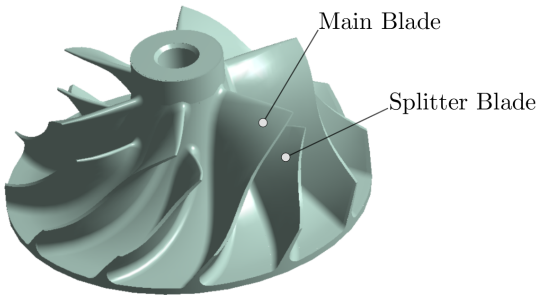

Figure 1: Baseline radial compressor with main- and splitter blades.

Table 1: Compressor geometric details

Number of blades	6+6
Inducer hub diameter	10 mm
Wheel diameter	40 mm
Inducer height	9.8 mm
Diffuser height	3 mm
Diffuser length	71 mm
Tip leakage gap	const. 0.3 mm

tipoint and multiobjective optimisation strategy, which directly couples a GA with a three-dimensional, steady state RANS analysis to perform a numerical optimisation of an automotive radial compressor. The procedure is applied to an automotive turbocharger compressor and the results for both baseline and optimised designs are validated through experimental testing. The compressor under investigation comprises six main- and splitter blades and is shown in Figure 1 along with details regarding the geometric sizing.

The optimisation procedure seeks to determine a global optimum of the objective function at a target optimisation region near surge, while simultaneously ensuring that the choke margin does not decrease below a certain, user-defined limit. This was applied to four different optimisation runs. The results of the initial two are compared with experimental data. Additionally, a flow field and loss analysis are carried out to determine reasons for enhanced performance.

2. Methodology

2.1. Numerical Method

The numerical analysis was done using the commercial software package ANSYS-CFX R16.1. The code solves the three-dimensional Reynolds-averaged Navier-Stokes (RANS) equations in a fully implicit manner using a hybrid finite-element/finite-volume discretisation approach. Throughout this study the flow is assumed to be fully turbulent with turbulence closure being ensured by Menter's k-ω SST model [30], which has proven to give accurate results when experiencing flow separation under adverse pressure gradients [31].

A converged solution is obtained as soon as the normalised root mean squared (RMS) residuals decrease below a threshold of 10^{-5} and domain imbalances have

dropped below 0.01. Furthermore, total-to-total isentropic efficiency and total pressure need to settle to stationary levels. Throughout this study, isentropic efficiency is evaluated as the ratio of the isentropic total enthalpy change to the actual total enthalpy change, while total pressure ratio is simply defined as the ratio of total pressures between domain out- and inlet. Total enthalpy is calculated via mass-flow averaged total temperature assuming constant specific heat capacity at constant pressure ($c_p = 1005 J/kg - K$) while pressure ratio is computed via mass flow averaged total pressures at domain in- and outlet.

The computational domain consists of three separate spatial regions. Broken down, this includes a stationary inlet pipe, a single passage (SP) domain housing impeller with main and splitter blades as well as diffuser and finally the volute, as shown in Figure 2. The respective fluid volumes were extracted from the original CAD model using Ansys BladeEditor and ANSYS Design Modeler. The impeller geometry was then simplified to facilitate the automatic meshing process during optimisation by removing fillets around the blades' hub and leakage cavities around the rotor geometry. The inlet pipe is extended sufficiently long to ensure enough distance between the domain inlet and possible recirculation regions. It also features the shape of the locknut. Both inlet pipe and single passage represent one sixth of the entire rotor and have periodic boundaries in azimuthal direction.

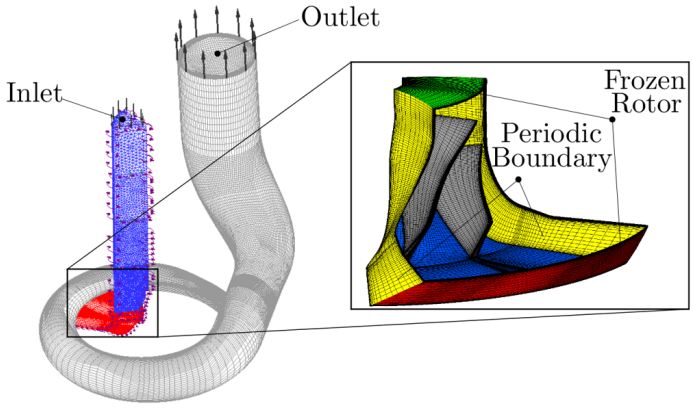

Figure 2: Computational domain including inlet pipe, single flow passage and volute.

The simulation is carried out in steady state using the false timestepping method implemented in CFX. The single passage region is set to a rotating frame of reference with a rotational speed of 180,000 rpm. Counter-rotating wall velocity is imposed to the diffuser and shroud wall rendering them stationary in the absolute frame of reference. Instead of using mixing or stage interfaces between the three distinct

regions, frozen rotor interfaces where selected, as this proved beneficial with respect to convergence for operating points close to surge [32]. However, this necessitates to ensure the fixed relative position between volute and single passage does not produce erroneous results, which was achieved by running full rotor simulations at operating points near surge, peak efficiency and near choke and comparing the global variables of isentropic efficiency and total pressure ratio.

In terms of boundary conditions stagnation properties are imposed at the inlet. These comply with the ambient conditions present at the time of experimental testing (around 99.6 kPa and 298 K). At the outlet, a mass flow condition is set, again in accordance with the conditions met during testing. Walls are treated as hydraulically smooth and adiabatic with a no-slip condition. Air is considered as a calorically perfect gas. A summary of the computational setup is given in Table 2.

Table 2: Numerical setup for the steady CFD computations.

Analysis Type	Steady state
Impeller Speed	180,000 rpm
Medium	Air, calorically perfect gas
Walls	Adiabatic, hydraulically smooth
Inlet	Stagnation temperature and pressure
Outlet	Mass flow outlet
Interface	Frozen rotor
Turbulence Model	Menter's $k-\omega$ SST
Advection Scheme	High resolution
Turbulence Numerics	High resolution

2.1.1. Domain Discretisation and Mesh Independence

Each of the three regions was meshed separately. Firstly, the numerical grids of inlet pipe and volute remain constant throughout the study. For the former, an unstructured grid consisting of 300,000 tetrahedral elements was generated using ANSYS MESHING. Near wall gradients are resolved using six prismatic elements. The volute mesh was discretised in ANSYS ICEM using a block-structured approach. It comprises around 500,000 hexahedral elements with a minimum quality of 0.40. To obtain a good balance between computational accuracy and resource intensity the average non-dimensional distance of the first cell $\bar{y}^+$ at an operating point near surge is 32, so that near wall gradients are accounted for through the automatic near-wall

treatment. For the mesh of the single passage, a block-structured grid is generated using ANSYS TURBOGRID. This ensures a high quality mesh and facilitates the automatic meshing procedure necessary for geometry changes in the optimisation study.

Discretisation of the domain incurs an error that needs to be quantified in order to gain fidelity in the simulation results. To do so, this paper follows the procedure introduced by Celik [33]. The impeller/diffuser region is the most sensitive region where the majority of pressure increase takes place and is thus chosen for the mesh study. Three distinct grid sizes (coarse, medium and fine) where generated and were then run at different operating points along a single speedline and compared against experimental data. Table 3 summarises the mesh statistics and respective quality metrics for the mesh sensitivity study.

Table 3: Mesh statistics and quality of the impeller grids for the mesh independence study.

Mesh	SP cell No.	Tot. cell no.	$\overline{y}^+$	Min. face angle	Max. element vol. ratio
Coarse	$0.18 \cdot 10^6$	$0.98 \cdot 10^6$	19	19.62	34.1
Medium	$0.64 \cdot 10^6$	$1.44 \cdot 10^6$	3	21.61	23.9
Fine	$1.14 \cdot 10^6$	$1.94 \cdot 10^6$	1.9	21.33	26.9

2.2. Optimisation Method

In general, one can formulate an optimisation problem as

$$\begin{aligned} \text{Min.} \quad & OF = OF(P(X_i), X_i), \qquad \text{with } \mathrm{X_i}(1, 2, .., \mathrm{n}); \\ & X_i^{lb} \leq X_i \leq X_i^{ub} \end{aligned} \tag{1}$$

The aim of any optimisation is to minimise an objective function (OF) that is a function of n design variables $\mathrm{X_i}$ and the performance parameters $\mathrm{P(X_i)}$. Design variables are usually subject to certain constraints and are allowed to vary between a lower and an upper limit. The objective function can be any linear combination of differently weighted penalties.

The optimisation routine followed in this study employs a standard elitist genetic algorithm (GA) implemented in Matlab R2016b. The population size was fixed to a minimum number of twice the number of geometric parameters. Earlier trial runs indicated this to give acceptable convergence rates and proved to be an acceptable compromise between the computational expense and optimisation accuracy. Nonetheless, it is important to point out that required size of the initial population and each generations can vary depending on the problem at hand.

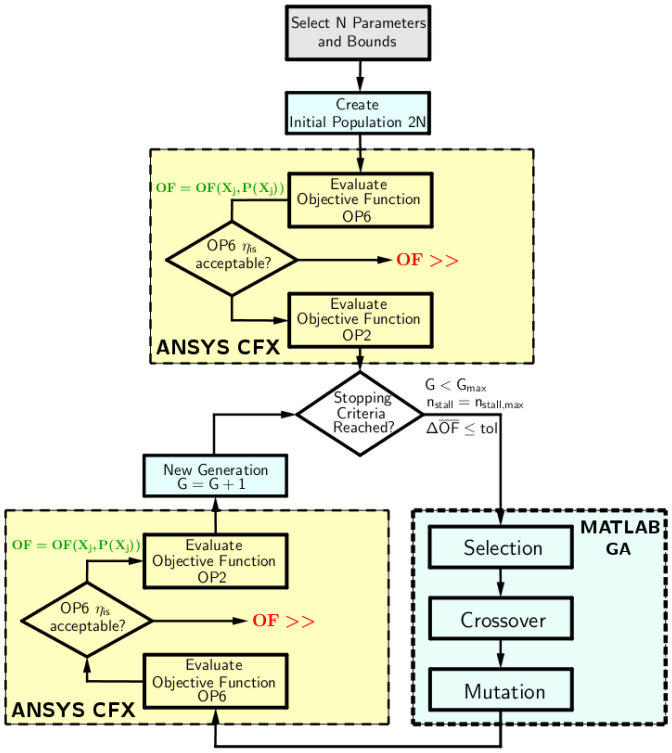

Figure 3: Flow chart of optimization procedure coupling GA and 3D-CFD.

In general, the GA creates subsequent generations of design points through elitist selection, crossover and mutation. In this study, the best two candidate designs are always carried over to the next generation, while a crossover fraction of 0.8 defines the offspring created through exchange of genetic material. For parent selection the default stochastic uniform technique was used. The remaining design points are selected through mutation ensuring the search does not get trapped in a local minimum. Mutation is accomplished through random generation of directions within the design space. Optimisation runs are stopped either as soon as the maximum number of generations (15) is reached, the relative change in the average penalty value between two following generations falling below 10^{-6} or the best fitness value does not change within the last three generations. The maximum number of generations was set based on initial optimisation runs and proved to be sufficiently large in order to yield a converged result.

A flowchart outlining the multipoint optimisation performed in this study is shown in Figure 3. The main optimisation seeks to maximise efficiency in the operating region near surge, while ensuring the choke margin does not drop below a

certain threshold. The target optimisation point, referred to as OP2 was selected. It is slightly offset from the surge line in order to ensure acceptable numerical convergence during simulation. OP6 is selected as the operating point, where the behaviour near choke is investigated. Before the routine can commence, it is necessary to select the relevant design variables, decide on their range and parameterise the underlying geometry. Blade shapes are defined by the three camberlines (hub, midspan, shroud). These camberlines are approximated via Bezier curves using three control points (leading edge, centre, trailing edge). This gives full control over the blade shape at both hub and shroud. Furthermore, the flow path contour is controlled via a Bezier curve of three control points that defines the hub shape . Additionally, blade length and sweep angle can be varied via respective control points. After having selected N design variables and parameterising the geometry, MATLAB creates an initial population that spans the search space. First of all, design points in the initial generation run at OP6 near choke first. Those design points whose isentropic efficiency does not fall short of the specified threshold are then carried over to be run at the target optimisation point, OP2. Here, the objective function assigned to each design point is a function of the isentropic efficiency at OP2. If the isentropic efficiency at OP6 does not comply with the required level, a large penalty value is assigned.

As soon as the initial population is solved, the Matlab GA creates a new generation using the previously described mechanisms of selection, crossover and mutation.

2.2.1. Initial Optimisation Campaigns

For the first optimisation run, the impeller geometry was parameterised using 13 design variables. Two control points at midspan and near the shroud are used to vary the leading edge blade shape, with two control points on each blade control the change in backsweep and stacking or leaning angle. Additionally, pitch fraction is also allowed to vary. A single control point governs the hub contour, while two control points manipulate splitter length and sweep angle. Finally, one single control point at the leading edge manages the main blade sweep angle. Diffuser height, impeller outer diameter as well as blade number were fixed.

The second optimisation run was split in two steps. First, a DoE was conducted using the Box-Behnken approach considering a total number of seven parameters, as shown in Figure 4(a). The DoE was limited to a single operating point (OP2) and 7 design parameters ((Figure 4(b)). However, since the onset of choke is mostly associated with flow blockage, the splitter length was reduced in order to limit the reduction in choke margin by the response surface optimisation. Furthermore, pitch fraction was varied slightly, such that the splitter blade is moved towards the main

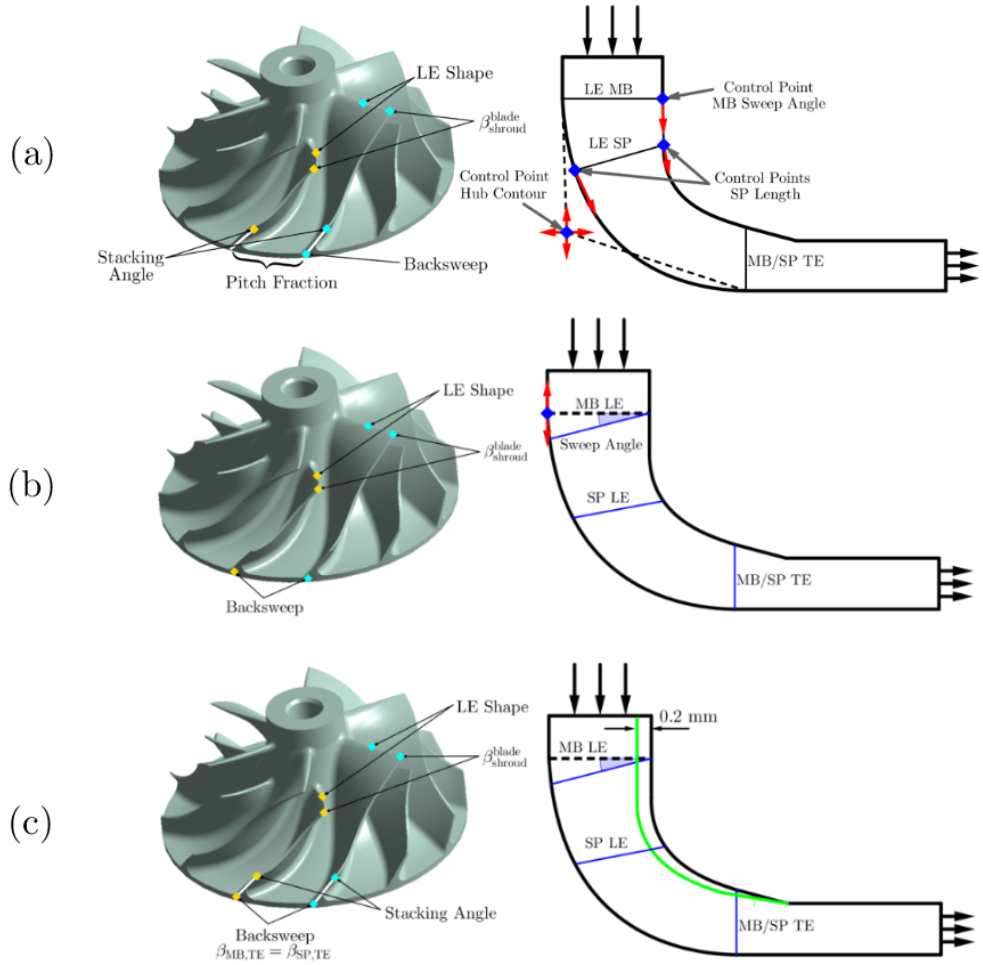

Figure 4: Optim1 geometry parameterisation of blade shape and flow path considering 13 different variables.

blade suction side, as initial simulations implied a favourable effect on isentropic efficiency. This optimisation was conducted using a MOGA technique aimed at maximising both pressure ratio and isentropic efficiency. The best design candidate then was trimmed at the shroud by 0.2 mm at the inducer. A subsequent GA optimisation focused on the blade shape (Figure 4(c)) of splitter and main blade, with backsweep set equal on all blades. The same objective function as for Optim1 was used. The objective function for both optimisation runs is given in Equation 2.

Table 4: Lower and upper bounds for design variables for Optim1 and Optim2. The first value denotes the upper bound and the lower value the lower bound. All values are given relative to their original state.

Parameter	Parameter bounds Optim1	Parameter bounds Optim2 - DoE	Parameter bounds Optim2 - GA
Hub − h	$+2.5\text{mm}/-0.5\text{mm}$	-	-
Hub − v	$+2.5\text{mm}/-0.5\text{mm}$	-	-
MB sweep	$+1\text{mm}/-2\text{mm}$	$+2\text{mm}\ +4\text{mm}$	-
SP length shroud	$-3.1\text{mm}/-6.0\text{mm}$	-	-
SP length hub	$-2.0\text{mm}/-3.0\text{mm}$	-	-
MB $\beta_{\text{LE,shroud}}$	$+1°/-8°$	$+8°/-9°$	$+4°/-4°$
MB $\beta_{\text{TE,shroud}}$	$+4°/-0.5°$	-	$+6°/+0.5°$
MB $\beta_{\text{TE,hub}}$	-9°/−15°	$+8°/-9°$	$+2°/-5°$
SP $\beta_{\text{LE,shroud}}$	$+4°/+15°$	$+5°/+4°$	$+4°/-4°$
SP $\beta_{\text{TE,shroud}}$	$+4°/-0.5°$	-	$+6°/-0.5°$
SP $\beta_{\text{TE,hub}}$	-	$+4°/-4°$	= MB $\beta_{\text{TE,hub}}$
MB β_{LEshape}	$-4°/-6°$	$+4°/-4°$	$+3°/-3°$
SP β_{LEshape}	$+3°/-5°$	$+4°/-4°$	$+3°/-3°$
Pitchfraction	0.61/0.51	-	-

$$OF_{\text{Optim1},Optim2}(X_i) = \begin{cases} -100 \cdot \eta_{\text{OP2}}, & \eta_{\text{OP6}} \geq 0.925 \cdot \eta^{BL}_{\text{OP6}} \\ 10 - 5 \cdot \eta_{\text{OP6}} & \eta_{\text{OP6}} < 0.925 \cdot \eta^{BL}_{\text{OP6}} \end{cases} \tag{2}$$

A summary of all considered variables and their respective upper and lower bounds is given in Table 4. It is noteworthy that all values are given relative to their original value. Upper and lower limits were determined by initial DoE runs of the parameters investigating their potential for performance improvement and the requirement manufacture potential design candidates by the same standard flank milling method as the baseline model.

2.3. Revised Optimisation Campaign

To account for the detrimental effect adverse blade loading imparts on the operating width while maximising solely for efficiency, two alternative optimisation procedures are proposed. The first one, referred to as Optim3, includes blade loading in the objective function, as seen in Equation 4. The weighting factors are chosen such that isentropic efficiency and loading unbalance are weighted the most, while the contribution of Mach peak and negative loading is comparably smaller. They read $\text{w}_1 = 300,\ \text{w2} = 100,\ \text{w}_3 = 10$ and $\text{w}_4 = 2.5$. The efficiency penalty was altered such that it penalises the difference between the computed efficiency and its difference to the target efficiency (set to a 100%).

$$
\begin{aligned}
P_{\eta,\mathrm{OP2}}(X_i) &= \eta_{\mathrm{target}} - \eta_{\mathrm{OP2}}(X_i) \\
P_{\eta,\mathrm{OP6}}(X_i) &= 250 - 50 \cdot \eta_{\mathrm{OP6}}(X_i)
\end{aligned}
\tag{3}
$$

The target for OP6 was reduced and now allows a reduction in efficiency of 10%. Concerning the geometric parameters, both main blade and splitter lengths are allowed to vary in both directions as well as relative blade angle at the leading edge near the shroud. At the trailing edge backsweep and stacking angle are allowed to vary, too. The centre camberline was ignored and, as pitch fraction has shown to exacerbate loading unbalance, pitch fraction is fixed at 0.5. In total, eleven parameters are considered, as highlighted in Figure 6(a). Defining a penalty function that includes blade loading confirms an adverse blade loading that adds to a reduction in surge margin. The penalty function reads

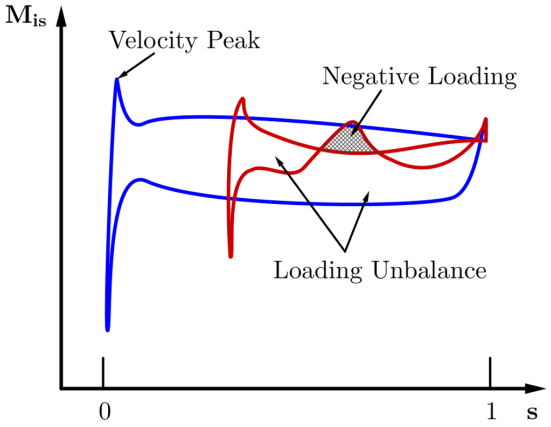

$$
\begin{aligned}
P_{LU} &= \left(\frac{A_{BL} - A_{SP}}{A_{BL} + A_{SP}}\right)^2 \\
P_{MP} &= \int_0^1 \max\left[M_{is,ps}(s) - M_{is,ss}(s), 0\right]\mathrm{ds} \\
P_{NL} &= \max\left[\Delta M_{is,ss-ps}(LE)\right]
\end{aligned}
\tag{4}
$$

Figure 5: Blade loading schematic between main blade (blue) and splitter blade (red).

$$
\mathrm{OF}_{\mathrm{Optim3}}(X_i) = \begin{cases} w_1 P_{\eta,\mathrm{OP2}}(X_i) + w_2 P_{\mathrm{LU}}(X_i) + w_3 P_{\mathrm{MP}}(X_i) + w_4 P_{\mathrm{NL}}(X_i), & \eta_{\mathrm{OP6}} \geq 0.90\eta_{\mathrm{OP6}}^{\mathrm{BL}} \\ P_{\eta,\mathrm{OP6}}(X_i), & \eta_{\mathrm{OP6}} < 0.90\eta_{\mathrm{OP6}}^{\mathrm{BL}} \end{cases} \tag{5}
$$

For the second revised optimisation - labelled Optim4 - a different approach is chosen. To eradicate the effect of loading unbalance and possible unfavourable interaction between splitter and main blade, it was decided to investigate the compressor performance without a splitter. In theory, the number of blades determines the flow distribution at the exducer and the slip factor. A larger number of blades reduces slip and thus the difference in the velocity profile from an ideal with good flow guidance.

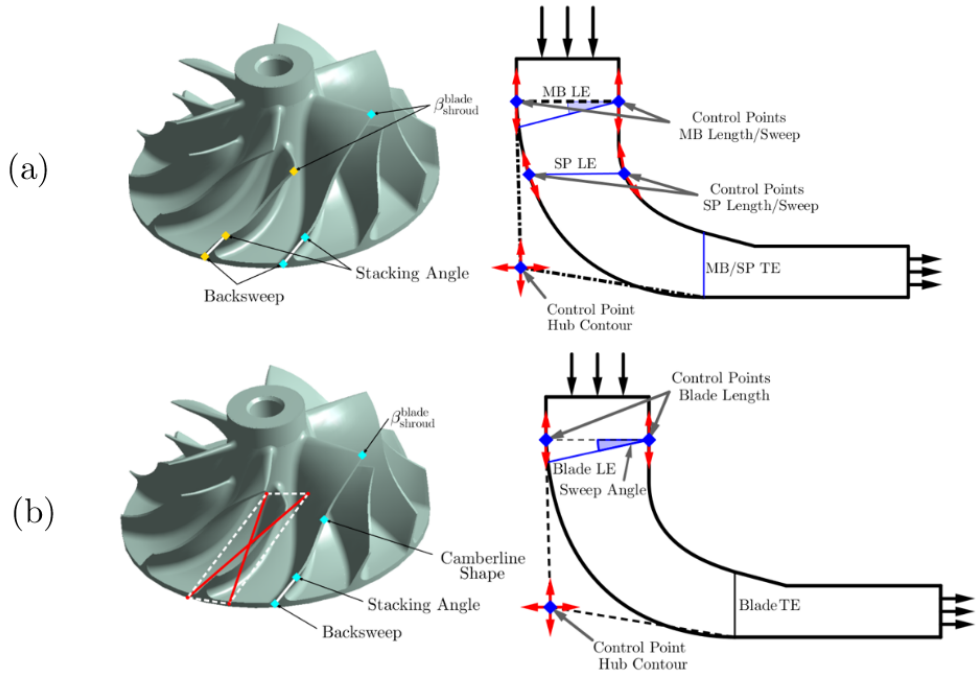

Figure 6: Optim3 geometry parameterisation for (a) DoE and (b) GA considering eleven different variables each.

However, a larger number of blades reduces the choke margin as the passage width between blades is reduced. At first, a small DoE was conducted on the baseline design without splitters using the number of blades as the sole parameter and letting it vary from six to eleven. This of course cannot capture how the modification of other parameters might compensate for a change in blade number, but should give an indication of what number of blades is necessary to be within the required performance limits.

Given the baseline main blade design and hub and shroud contour, nine or ten blades appear most feasible as given in Table 5. The former has a higher efficiency at OP6 of 2.6 pp while the former a slight decrease of 0.93 pp. It was thus decided to proceed with nine blades and allow the optimisation procedure to have more flexibility at OP2. The same objective function as for Optim1 and Optim2 was used considering eleven parameters, displayed in Figure 6(b). This includes backsweep, stacking angle, the shroud relative blade angle as well as the blade shape at hub and shroud. Blade length, sweep angle as well as flow path shape are included in the optimisation as well. A summary of the parameters and their constraints is shown in Table 6.

Table 5: Change in efficiency near choke (OP6) as a function of blade number.

Number of Blades	Efficiency Change $\Delta\eta$	Pressure Ratio Change $\Delta\Pi$
6	+7.8 pp	+5.9%
7	+7.0 pp	+4.4%
8	+3.9 pp	+2.3%
9	+2.6 pp	+1.6%
10	−0.9 pp	−1.7%
11	−6.2 pp	−5.6%

$$\mathrm{OF}_{\mathrm{Optim4}}(X_i) = \begin{cases} -w_1 P_{\eta,\mathrm{OP2}}(X_i), & \eta_{\mathrm{OP6}} \geq 0.90\eta^{BL}_{\mathrm{OP6}} \\ P_{\eta,\mathrm{OP6}}(X_i) & \eta_{\mathrm{OP6}} < 0.90\eta^{BL}_{\mathrm{OP6}} \end{cases} \tag{5}$$

Table 6: Lower and upper bounds for design variables of Optim3 and Optim4. The values denote upper and lower bound respectively. All values are given relative to their original state.

Parameter	Constraints Optim3	Constraints Optim4
Hub − h	+2.7mm/ − 0.6mm	+2.5mm/ − 0.5mm
Hub − v	+2.7mm/ − 0.6mm	+2.5mm/ − 0.5mm
MB length shroud	+1.3mm/ − 2.5mm	+1mm − 2mm
MB length hub	+1.3mm/ − 2.5mm	+1mm − 2mm
SP length shroud	+0.5mm/ − 0.5mm	-
SP length hub	+0.7mm/ − 2.0mm	-
MB $\beta_{\mathrm{LE,shroud}}$	$+1°/-10°$	$+1°/-9°$
MB $\beta_{\mathrm{TE,shroud}}$	$+10°/-0.5°$	$+10°/0°$
MB midchord, hub	-	$+0.1/-0.1$
MB $\beta_{\mathrm{midchord,hub}}$	-	$+15°/+25°$
MB midchord, shroud	-	$+0.25/-0.25$
MB $\beta_{\mathrm{midchord,shroud}}$	-	$+10°/-10°$
MB $\beta_{\mathrm{TE,hub}}$	$+1°/-11°$	$+1°/-9°$
SP $\beta_{\mathrm{LE,shroud}}$	$+6°/-12°$	-
SP $\beta_{\mathrm{TE,shroud}}$	$+10°/-0.5°$	-

2.4. Experimental Setup

The University of Bath turbocharger test rig, developed at the Powertrain and Vehicle Research Centre (PVRC), was used to validate the baseline model, as well as the optimised geometries Optim1 and Optim2 and create compressor performance maps.

The gas stand is comprised of three modules, namely compressor, turbine and lubrication module. A schematic highlighting components is given in Figure 7. Each

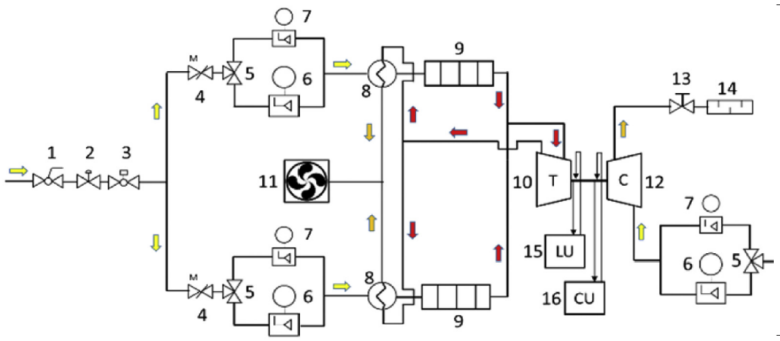

Number	Unit
1	Manual ball type shut-off valve
2	Pneumatic pressure regulator
3	Electro-pneumatic positioned ball type valve
4	Motorised butterfly valve
5	Three-way ball type valve
6	3" McCrometer V-cone mass flow meter Siemens DSIII dp-sensor
7	2" McCrometer V-cone mass flow meter Siemens DSIII dp-sensor
8	Gas-gas heat exchanger
9	44kW electric heater
10	Turbine
11	Extraction fan
12	Compressor
13	Pneumatically controlled backpressure valve
14	Performance silencer
15	Lubrication unit
16	Water cooling unit

Figure 7: Turbocharger gas stand schematic.

consists of a separate piping system. When operated as an open loop system, air is drawn from the ambient through the compressor before being passed through a pneumatically actuated gate valve and a silencer (elements 13 and 14 respectively). Modulation of the gate valve insert allows controlling compressor pressure ratio and power developed by the compressor and allows testing of surge at low mass flow rates.

The turbine module draws compressed and dehumidified air (up to 7 bar absolute) from a set of rotary type industrial compressors through a pair of 44kW electrical heaters (elements 9). In addition, an air-to-air recuperation system (elements 8) preheats the incoming turbine feed air before being directed through the heaters. After passing through the heat exchangers the air is expelled through a fan controlled air extraction system (elements 11). The turbine feed system can deliver a maximum temperature of around 750° C. However, the turbine inlet temperature during testing is at 600° C. To ensure little heat loss between heaters and turbine ducts are thermally insulated, while compressor ducts remain uninsulated throughout.

Finally, a lubrication system running at 90° C provides optimum conditions to the turbocharger bearings and removes heat from the turbocharger shaft assembly. In addition, the test facility features a water cooling circuit (fixed at 90° C) that allows to minimse the heat transfer between turbine and compressor side and ensure accurate determination of component efficiencies.

The steady-state measurements for pressure and temperature are done according to the SAE J1826 [34], SAE J1723 [35] and ASME [36] standards. This entails measuring average pressures on compressor and turbine in- and outlets using four pressure tappings. Similarly, mean static temperatures are computed using PRT's on compressor inlet and outlet and k-type thermocouples for turbine inlet and outlet.

Mass flow measurements on both turbocharger sides is done via McCrometer v-cone mass flow meters (elements 6 and 7). Differential pressure is measured via Siemens Sitrans DS III, while temperatures and pressures for density calculation are determined via PRT sensors and Omega pressure transducers.

The compressor maps depicted in this study were constructed through collecting around 7-10 data points along constant compressor rotational speed starting at high mass flow rates near choke and low pressure ratios moving towards low mass flow rates and high pressure ratios by adjusting the pneumatic gate valve downstream of the compressor, while turbocharger speed is controlled though the mass flow rate and delivery pressure to the turbine.

3. Results and Discussion

3.1. Mesh Sensitivity Study

For model validation, the numerical model was run along the 180,000 rpm speedline. The results for isentropic efficiency and total pressure ratio were compared with the experimental data yielding the graphs shown in Figure 8. The speedline was divided into seven operating points (labelled from OP1 to OP7) corresponding to the boundary conditions logged during experimental testing of the compressor. The discrete points denote the numerical data, while the black dashed line gives a least squares curve of the experimental data points. The numerical results indicate a slightly earlier onset of choke. Efficiency is moderately underpredicted for most operating conditions, while total pressure ratio is overpredicted. However, there is good overall agreement with the experimental data and trends are reasonably well predicted. Also, the use of the frozen rotor interface seems justified.

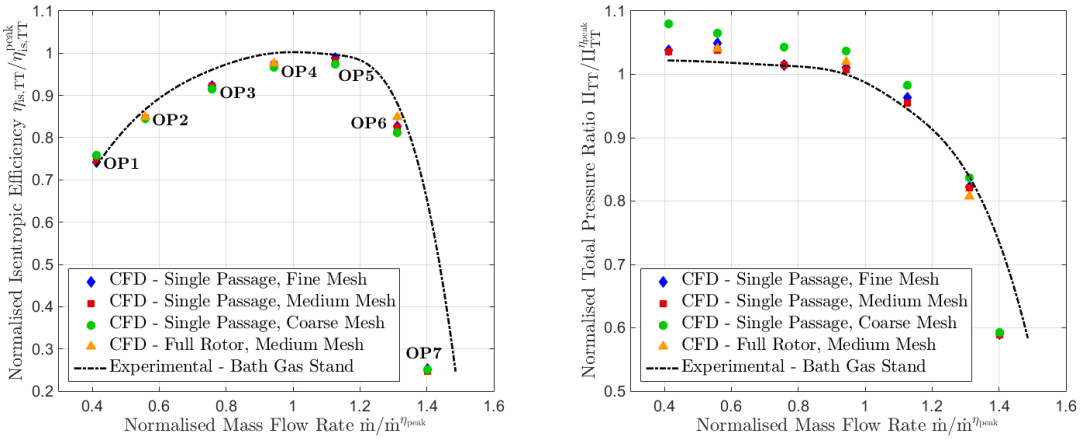

Figure 8: Comparison of CFD results for single passage and full rotor with experimental data for an impeller speed of 180,000 rpm

The summary of the grid convergence study is given in Table 8, reporting a grid convergence index for the medium mesh for efficiency and pressure ratio at off-design operating points, OP2 and OP6. This gives excellent results for global variables with all uncertainties for the medium mesh near choke and surge being below 2%.

Table 7: Discretisation error for efficiency and pressure ratio at operating points close to surge and choke respectively.

	$\eta_{\text{isen}}^{\text{OP2}}$	$\Pi_{\text{TT}}^{\text{OP2}}$	$\eta_{\text{isen}}^{\text{OP6}}$	$\Pi_{\text{TT}}^{\text{OP6}}$
r_{21}		1.32		
r_{32}		1.57		
p	4.1	2.2	4.1	5.3
e_{a}^{32}	0.3 %	2.6 %	1.7 %	2.0 %
e_{extr}^{32}	0.01 %	1.0 %	0.1 %	0.04 %
$\text{GCI}_{\text{medium}}^{32}$	0.1 %	1.9 %	0.4 %	0.3 %

Looking at blade loading distribution in Figure 9 of main blade and splitter at OP2 reveals little difference between the fine and medium mesh. This further indicates that the medium mesh provides an acceptable compromise between high accuracy and computational resource consumption and is therefore be used throughout the ensuing optimisation study.

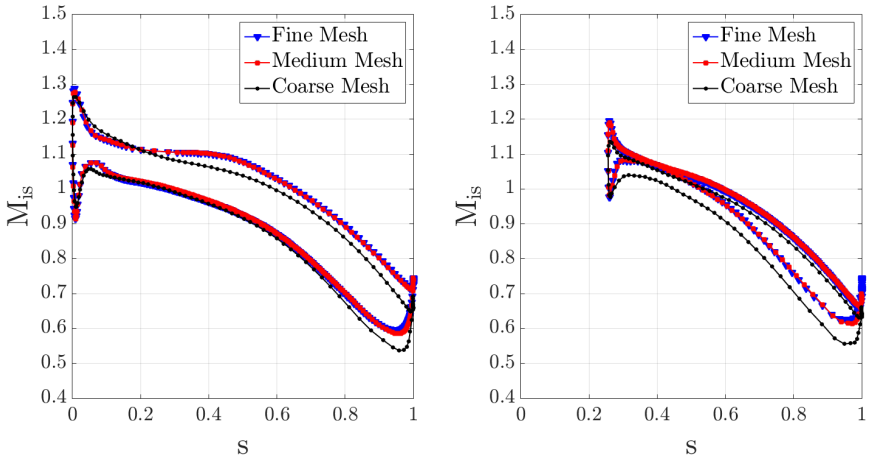

Figure 9: Blade loading near the shroud for main blade (left) and splitter (right) Results stem from off-design conditions (OP2) for coarse, medium and fine grids.

The normalised breakdown of entropy change is shown in Figure 10. Multiplying Gibbs entropy (assuming adiabtic conditions across the domain walls) with mass flow rate gives the entropy production rate $\dot{S}$. This equation can be easily implemented post-simulation. The envelope of the total entropy change highlights the relationship with isentropic efficiency with the minimum in entropy production being located near the peak efficiency points. The graph underlines that the impeller and diffuser losses constitute the major contributor to entropy production and thus the region

with the highest potential for improvement. Secondly, the losses in the inlet pipe increase towards lower mass flow rates as a consequence of a more pronounced flow recirculation forming near surge. Thirdly, it transpires that volute losses become increasingly important as one approaches choke. Therefore, if one is to make accurate predictions with respect to the choke margin, it is necessary to include the volute geometry.

In addition, due to the highly tangential flow at operating points near surge ANSYS CFX requires to enforce a uniform mass flux at the diffuser outlet in order to guarantee convergence [37]. This however, proved to yield erroneous flow conditions at the diffuser outlet that do not match the situation where the volute is included. It is thus concluded that the volute geometry be included at all off-design conditions in order make precise performance predictions.

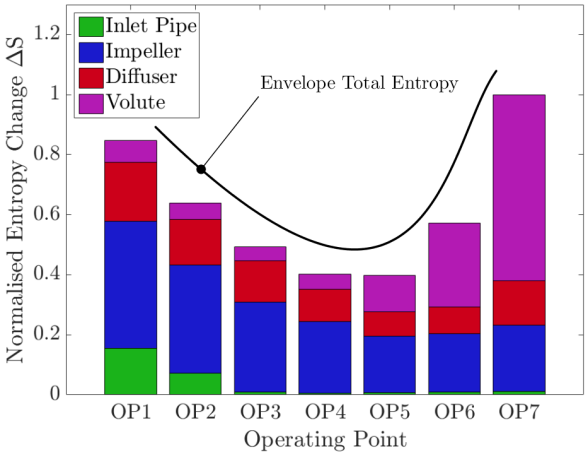

Figure 10: Break down of entropy generation for at each section (inlet pipe, impeller, diffuser and volute) along a single speedline of 180,000 rpm.

3.2. Optimisation Results

The design optimisation of Optim1 spanned eight generations with 280 different designs considered. In total, 508 CFD simulations were conducted. The DoE for Optim2 included 62 simulations, while the subsequent GA produced seven generations dealing with 135 different designs and a total number of 192 CFD simulations. Each design point claims approximately one hour to perform geometry and mesh update and run the simulation on a single node with a 24 physical core Intel Xeon E5 3.40 GhZ processor.

Figure 11 shows the Pareto optimal front for (a) Optim1 and (c) Optim2. It

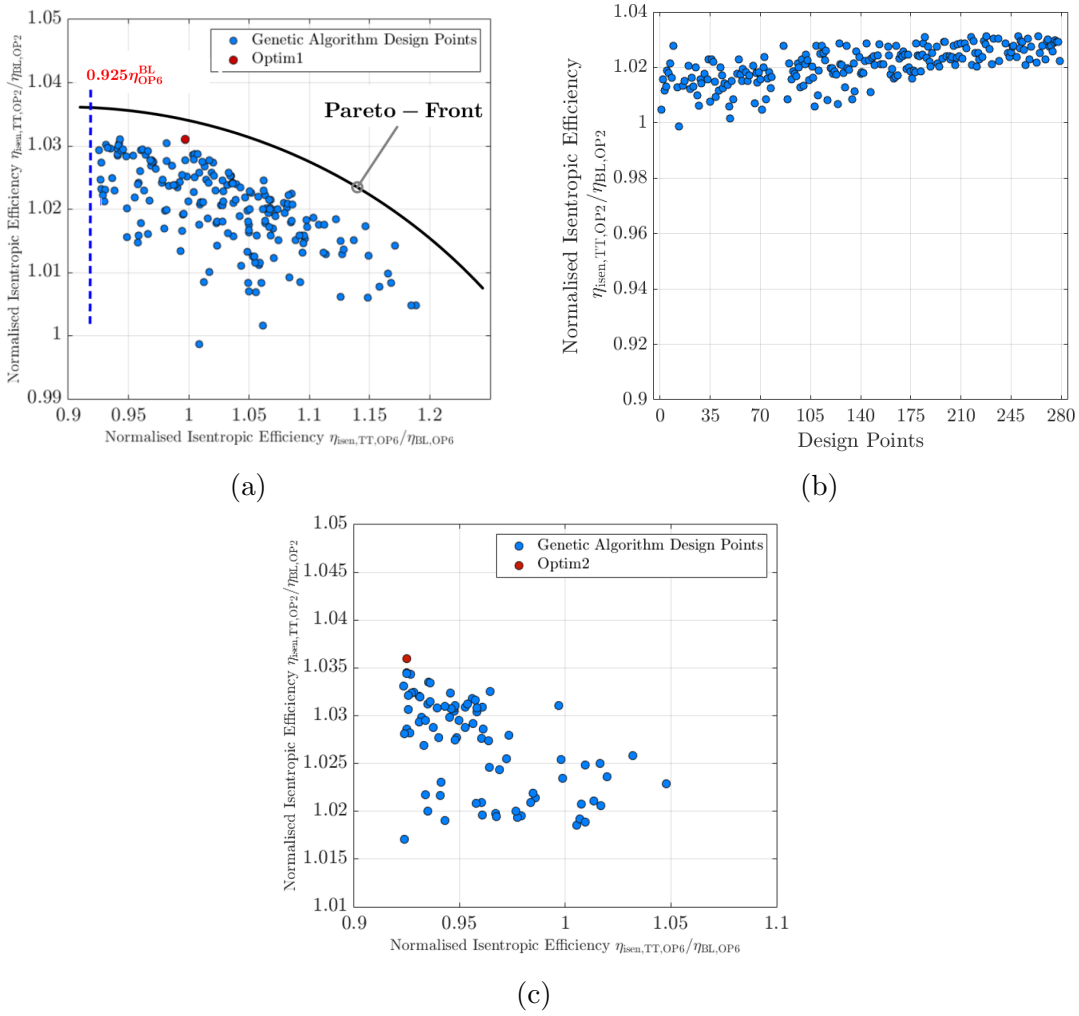

Figure 11: Pareto optimal front for normalised isentropic efficiency at OP6 and OP2 for (a) Optim1 and (b) Optim2. The selected candidate designs are shown in red.

further shows the progression of the efficiency at OP2 with every design evaluation. The Pareto front underlines the trade-off relationship between efficiency near choke and near surge. It shows that in order to obtain high efficiency in the target optimisation region, some relaxation with respect to the drop in choke margin needs to be made. The best candidate design for Optim1 indicates an efficiency improvement of 1.9 percentage points (pp), with the choke margin being reduced by merely 0.2 pp.

As far as Optim2 is concerned, the response surface optimisation yielded a design giving 1.7 pp efficiency improvement and as a result of the reduced splitter length

and thus reduced blockage an increase in efficiency near choke of around 2 pp. The optimisation then sacrificed the increase in choke margin to give an efficiency gain of 2.2 pp at OP2.

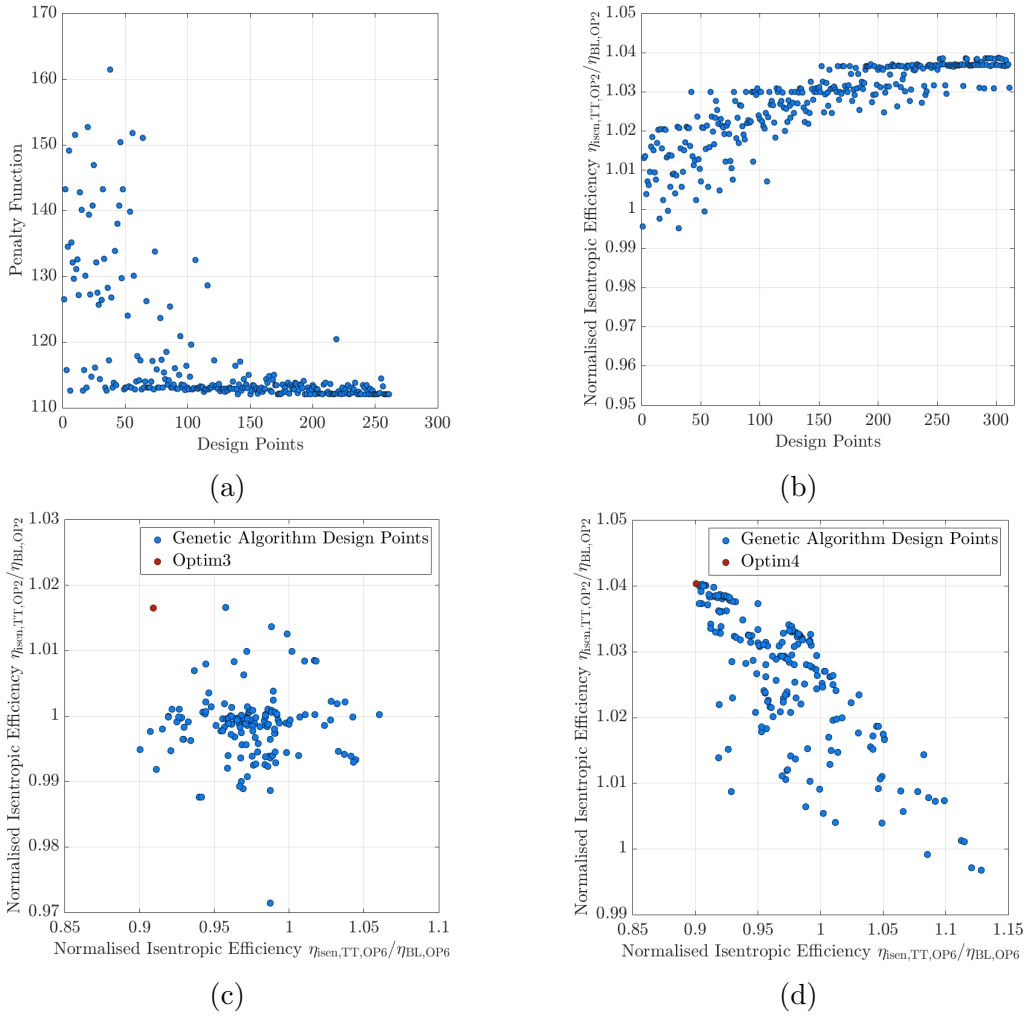

Figure 12: Optimisation results showing convergence of penalty function for (a) Optim3 and (b) Optim4. The relationship between performance near choke (OP6) and near surge (OP2) is given in (c) and (d).

The design optimisation of Optim3 converged after 13 generations with 286 different designs being investigated. A total number of 549 CFD simulations were carried out. The optimisation on the splitterless geometry Optim4 took 16 generations and

352 different design variants resutling in 622 CFD simulations.

The convergence of both cases is depicted in Figure 12 (a) and (c). The two graphs illustrate how the respective objective function settle down after initially showing a large spread as more and more design candidates and generations are simulated. There remain a number of outliers until the end of the optimisation, which can be attributed to mutation. Comparing Figure 12 (b) the effect of including blade loading in the objective function on the relationship between the efficiency at the two considered operating points across the speedline begins to show. The majority of design points are centred around the same efficiency as the baseline model, while choke margin efficiency decreases slightly. The candidate design picked is not the design with the lowest blade loading penalty, as this would not improve the efficiency at OP2. The chosen design, however,indicates a 1.1 pp increase in isentropic efficiency at OP2 and a 1.6 pp decrease in efficiency at OP6.

In contrast to Optim3, the same Pareto optimal front as already seen in the optimisation runs of Optim1 and Optim2 is also seen in Figure 12 (d). Here, the best efficiency indicates an efficiency improvement of 2 pp, while OP6 efficiency decreases by 4.9 pp.

3.3. Experimental Results

Testing baseline, Optim1 and Optim2 on the water-cooled turbocharger gas stand at the University of Bath yields the compressor maps plotting corrected mass flow rate versus total pressure ratio with corresponding normalised efficiency islands as shown in Figure 13. Isentropic efficiencies are normalised by the peak efficiency of the baseline model. The corresponding corrected mass flow rate and total pressure ratio at peak efficiency are used to normalise the remaining variables. The maps show speedlines ranging from 80,000 to 220,000 rpm.

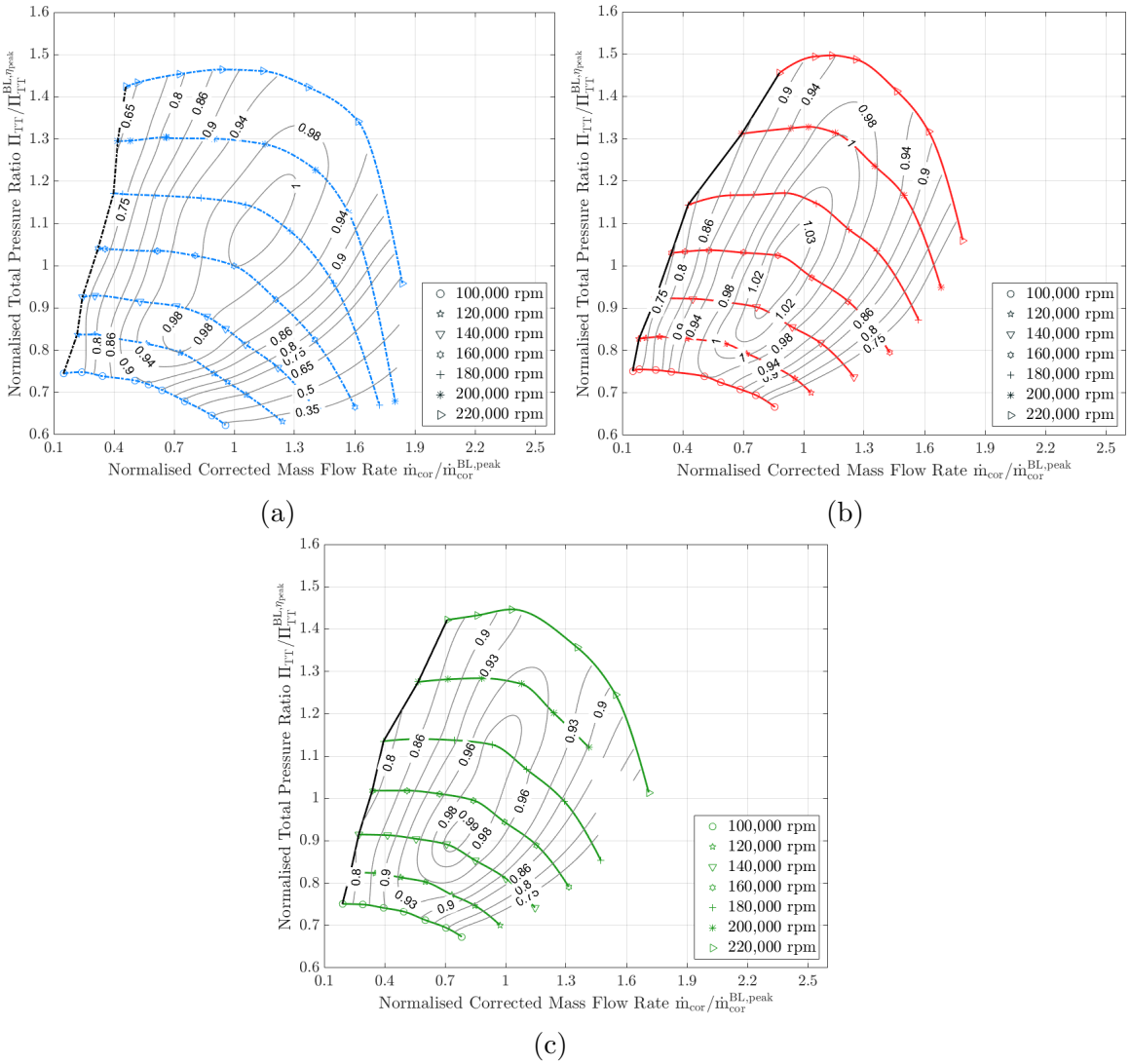

Figure 13: Experimental data showing compressor performance maps including iso-curves for isentropic for (a) baseline, (b) Optim1 and (c) Optim2.

Towards lower mass flow rates the plots show the hard surge line. In the absence of a general definition of hard surge and a myriad of varying definitions of mild surge, this study focuses on hard surge, which in this study is defined by a peak-to-peak pressure amplitude of 50 kPa and a frequency of around 8-10 Hz.

Pertaining to Optim1, up to around 180,000 rpm the hard surge margin remains similar, with a slight reduction in surge margin at 180,000 rpm. For higher rotational speeds, there is, however, a marked decrease in the hard surge line. Optim2

demonstrates a mildly larger surge margin up to 180,000 rpm, a virtually unchanged surge margin at 180,000 rpm and again a pronounced reduction for higher impeller speeds. The better performance near surge is partly down to trimming, as this shifts the map towards lower mass flow rates.

As far as efficiency is concerned, Optim1 achieves a higher peak efficiency, which can be reported as an increase of 3 pp. The peak efficiency island is shifted towards lower mass flow rates and pressure ratios. The target optimisation region benefits from this improvement and exhibits a higher efficiency as well. Optim2 shows a similar peak efficiency, which, as a result of trimming, moved towards lower mass flow rates and also towards lower pressure ratios of around 1.6. In the target optimisation region an increase in efficiency can be seen.

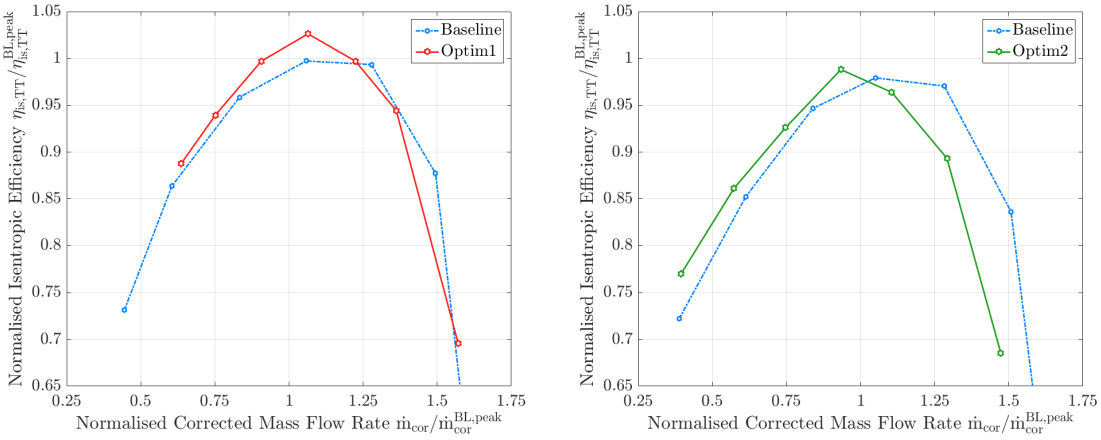

(a) (b)

Figure 14: Experimentally determined isentropic efficiency of 180,000 rpm speedline comparing baseline model with (a) Optim1 and (b) Optim2.

Extracting data for a single speedline of 180,000 rpm and comparing baseline with the optimised versions, confirms an increase in efficiency of approximately 1-2 pp near OP2. Furthermore, the experimental data substantiates the finding of the numerical analysis that the choke margin remains virtually unchanged. The speedline comparison for Optim2 illustrates the effect of trimming with a shift in peak efficiency towards lower mass flow rates and a slight increase of around 1 pp. In the proximity of OP2 an increase of around 2 pp can be reported. The choke margin reduces by around 0.005 kg/s as seen at a normalised efficiency level of 0.67.

The experimental tests therefore agree well the findings of the GA as far as the

efficiency improvement and the shift of the choke line are concerned, despite a shift in surge margin, which becomes particularly pronounced for higher impeller speeds.

3.4. Blade Loading Analysis

Despite good agreement with the results from the numerical analysis, the experimental data reveal a knock-on effect of the shape optimisation on the onset of surge. The inadequacy of steady state CFD simulations to predict the onset of surge is well established and documented [38, 39]. Nonetheless, van den Braembussche [40] implies that favourable blade loading can serve as an indicator of operating range width and thus at the onset of surge.

Table 8: Blade loading penalty for baseline, Optim1 and Optim2.

Model	Negative Loading	Mach Peak	Loading Unbalance	Penalty Shroud	Penalty Overall
Baseline	0.42	0.78	0.99	52.8	108
Optim1	0.04	0.97	1.80	76.1	190
Optim2	0.04	0.84	1.43	55.6	152

Calculating the individual penalties, as done in Table 8 discloses that while negative loading is most pronounced in the baseline model, both Mach peak and loading unbalance exhibit lower penalties. Summation of these penalties near shroud, midspan and hub confirms a larger blade loading disadvantage for both Optim1 and Optim2. The results further comply with the experimental data as Optim1 suffers from the largest offset in surge margin compared with Optim2. Evaluating these blade loading profiles for baseline, Optim1 and Optim2 at hub, midspan and shroud at OP2 gives the corresponding distributions shown in Figure 15. Blade loading of the baseline model shows that main blades experience large velocity peaks at the leading edge at all stations from hub to shroud. Near the hub and midspan this also holds for the splitter, although the blade loading distribution downstream of the leading edge almost experiences negative loading. Near the shroud the splitter blade loading profile exhibits a large section of negative loading.

Looking at the corresponding distributions of Optim1 and Optim2 illustrates the reduction in splitter length of around 26% and 33%. What is more is that there is considerable loading unbalance between main blade and splitter, while main blade loading distributions appear to be similar with the exception of larger velocity peaks for Optim1.

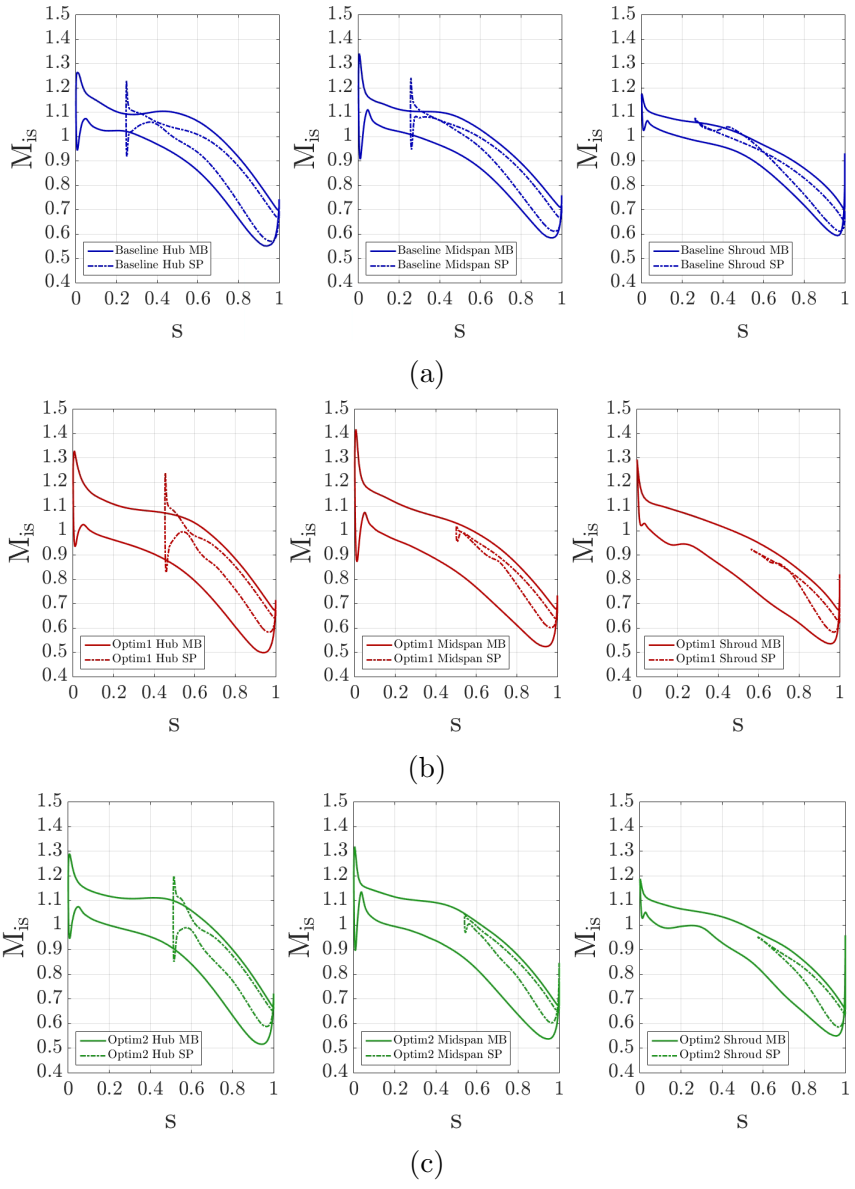

Figure 15: Blade loading distributions at hub (at 20 % span), midspan (at 50 % span) and shroud (at 80 % span) for (a) baseline, (b) Optim1 and (c) Optim2.

Blade loading profile from hub to shroud of Optim3 shows very similar results to the baseline model as far as the main blade is concerned, see Figure 16. The main change appears with respect to the splitter profile. Starting at the hub, the looming indication of negative loading just downstream of the leading edge in the baseline

model is no longer as pronounced, which results in no negative loading along the entire splitter surface with exception of a a very small negative loading region at the trailing edge, which renders the penalty very close but unequal to zero. Mach peaks seem to be slightly more pronounced on all sections as a consequence of the relatively low weighting factor assigned to it. It is expected that increasing this weighting factor will contribute to a lower velocity peak and a less strong deceleration thereafter.

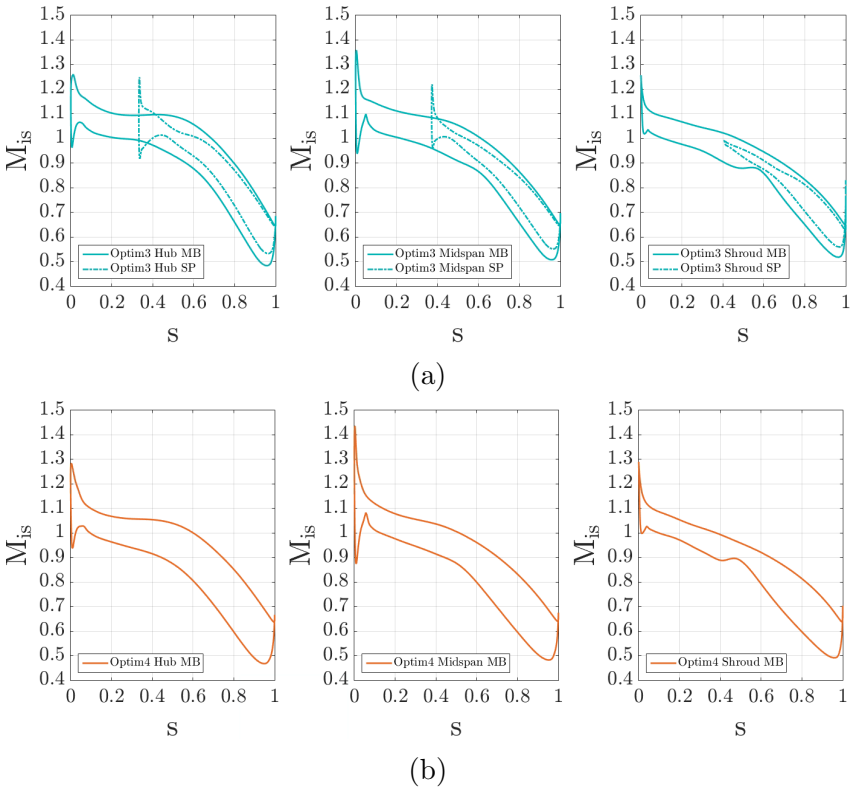

Figure 16: Blade loading distribution at hub, midspan and shroud for (a) Optim3 and (b) Optim4

Overall one can see a more even distribution between main blade and splitter, which mainly contributes to a considerably lower blade loading penalty compared with the baseline design, as shown in Table 9.

Pertaining to Optim4, a very similar distribution on the main blade can be reported. As already seen in the flow field analysis, larger Mach peaks are present, as it this is not included in the overall objective function. As loading unbalance is not of any relevance without a splitter, the resulting penalty - stated here for completeness - is low. This could be further improved by including a penalty for

velocity peaks along with a parameterised blade thickness distribution, although the resulting benefit may be offset by a decrease in efficiency improvement.

Table 9: Blade loading penalty for baseline, Optim3 and Optim4.

Model	Negative Loading	Mach Peak	Loading Unbalance	Penalty Shroud	Penalty Overall
Baseline	0.42	0.78	0.99	52.8	108
Optim3	0.02	1.02	0.62	29	70
Optim4	0.0	0.90	–	3	9

3.5. Entropy Generation Analysis

A loss examination based on local entropy generation rate and entropy production can give facilitate tracing of the reasons for performance gains. Evaluating entropy production rate over inlet pipe, impeller and diffuser and volute and comparing baseline geometry with the optimised models gives the breakdown of entropy production shown in Figure 17. The data is presented in normalised form with the total entropy production from the baseline selected as the normalisation factor.

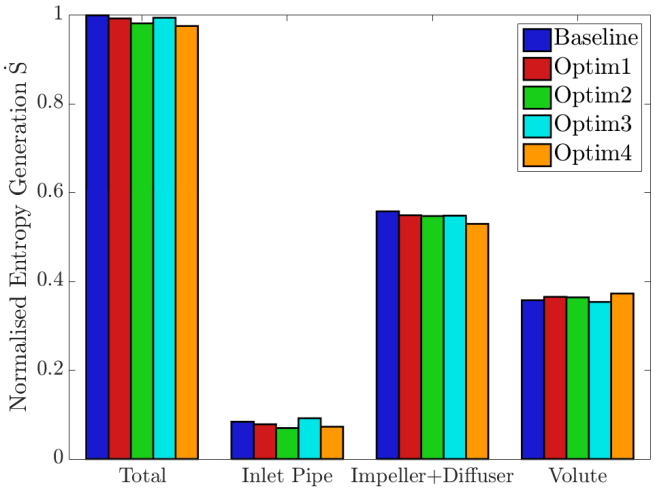

Figure 17: Comparison of entropy generation across the entire domain as well as across single sections for all design variants.

Near surge, around 6 to 9 % of the entropy production stems from the inlet, 35-38 percent from the volute and the majority (53-59 percent) from the impeller, indicating the highest potential for performance gains. The optimised geometries Optim1, Optim2 and Optim4 are characterised by lower irreversibility being generated across

inlet pipe, while Optim3 indicates a slightly higher loss generation upstream of the compressor, which offsets the gains made in the following impeller/diffuser section. All optimised geometries appear to have achieved lower irreversibility in the impeller and diffuser section, with Optim4 indicating the most pronounced improvement. However, larger average diffuser outlet velocities - with the exception for Optim3 - account for larger friction losses in the scroll that partially offset the performance gains made in the compressor section. Looking at the total entropy production it can be stated that the findings comply qualitatively with the results seen in the optimisation and in case of Optim1 and Optim2 also with the experimental data. The largest efficiency improvement is predicted for for Optim4 corresponding to a relatively lower entropy production. Nonetheless, the break-down illustrates the effect a change in geometry can impart on both up- and downstream components.

To facilitate the understanding of loss mechanisms on a local level, Denton [41], Kock and Herwig [42] and Iandoli and Sciubba [43] proposed the concept of local entropy generation rate. It decomposes losses into contributions through dissipation (i.e. shear induced) and heat transfer. It can be further differentiated in a mean-time term and a fluctuating (turbulent) term, so that the overall, local production term is given by Equation 6.

$$\dot{S}_{PROD} = \dot{S}_{PROD,\bar{D}} + \dot{S}_{PROD,D'} + \dot{S}_{PROD,\bar{C}} + \dot{S}_{l,C'} \tag{6}$$

It shall be noted that integrating Equation 6 across a domain should result in the same results as seen in Figure 17. However, several studies have pointed out that in reality they often do not, which is attributed to mesh resolution and the chosen turbulence model [44, 45]. Despite this discrepancy local entropy generation rate should give a good qualitative indication of loss generation mechanisms and has been used extensively in the past for turbomachinery [41, 42, 43, 44, 45].

The blade-to-blade (in the in θ-s plane) contour plots of Mach number and local entropy generation rate, as shown in in Figure 18, were evaluated at evaluation surfaces near the hub at 20% span length and allow a direction comparison between the baseline model and all optimised versions, (a) Optim1, (b) Optim2, (c) Optim3 and (d) Optim4. The normalisation factor was taken as the maximum entropy generation at the baseline diffuser-volute interface. An evaluation in vicinity of the hub was chosen as this clearly exemplifies the changes in loss characterisitic with respect to the baseline model while the differences appear to become more subtle as one approaches the shroud due to the proximity of the operating point to surge.

The flow field in the baseline model reveals a separation bubble (marked 1 in Figure 18) at the main blade suction surface close to the trailing edge. The splitter

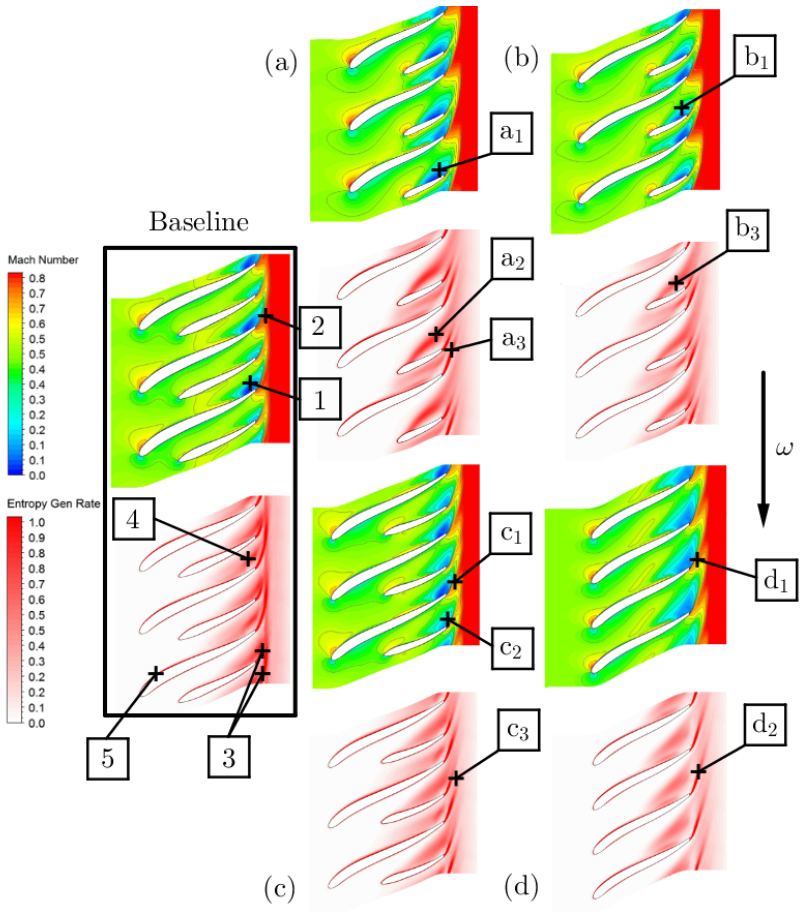

Figure 18: Break down of entropy generation for at each section (inlet pipe, impeller, diffuser and volute) along a single speedline of 180,000 rpm.

blade, however, exhibits only a very subtle low velocity region near the trailing edge on the suction side. Downstream of the trailing edge the wake flow (marked 2 in Figure 18) is characterised by a strong a shear flow, which is generated as a result of the convergence of a high momentum flow on the pressure side and the low momentum flow on the suction side. Looking at the entropy generation rates, it becomes clear that this shear flow accounts for large irreversibility being produced in the immediate wake region (marked 3 in Figure 18). Other contributors to entropy production involve the demarcation between the separation bubble and the flow encircling it (marked 4 in Figure 18), as well as the losses incurred in the boundary layer (marked 5 in Figure 18).

Comparing the flow field with Optim1 in Figure 18 (a) shows that the optimised

geometry features a shorter splitter length as well as a shift of the splitter towards the main blade suction side. One of the effects of these changes is a reduced size of the separated flow on the main blade suction side as more high momentum fluid is being directed along its surface, effectively delaying the onset of separation. However, this appears to come at the cost of a pronounced flow separation on the splitter suction side (marked a1 in Figure 18), resulting in higher losses near the separated zone and the wake region (marked a2 in Figure 18). Nonetheless, this drawback is compensated for by the reduced intensity of entropy production in the wake of the main blade (marked a3 in Figure 18), resulting in a higher overall efficiency. Optim2 features a similar splitter length as well as varied pitch fraction between main blade and splitter resulting in a similar flow field and loss characteristics as Optim1, albeit revealing a smaller extent of separation on the splitter suction side (marked b1 in Figure 18) causing less entropy generated in this zone (marked b2 in Figure 18) and giving higher efficiency.

Optim3 and splitterless Optim4 were aimed at tackling uneven blade loading distribution between splitter and main blade. The outcome of this study indicates a slightly reduced recirculation region on the main blade suction side and an increased separation on the splitter surface (marked c1 in Figure 18(c)). In a similar fashion to Optim1 and Optim2 this mitigated shear flow intensity in the wake region (marked c2 in Figure 18(c) and d1 in Figure 18(d)) stems from the reduced flow velocity coming from the blade pressure side that creates the trailing edge shear layer, ultimately resulting in lower entropy production (marked c3 in Figure 18(c) and d2 in Figure 18(d)).

4. Conclusions

This paper presented a numerical, multi-point optimisation of a radial compressor wheel using a combined CFD - GA approach. The objective of the study was to enhance the efficiency of an operating point near surge while ensuring the choke margin does not change significantly. In conclusion, the main points of this paper can be listed as followed:

- In order to perform multipoint optimsation on operating points close to the extremities of the performance map and obtain accurate performance predictions it is vital not to limit the computational domain to the impeller and diffuser section only, but to include the volute geometry. This proves particularly important near choke, where volute losses form a significant portion of total losses.

- In the process, four optimisation studies were executed, with a projected performance benefit of around 1.2 to 2.0 pp in the target optimisation region. For the first two optimisation studies, experimental testing was conducted that confirmed the performance benefit, albeit predicting lower increments. Experimental validation leads to the conclusion that the achieved values match the numerical results well and clear performance benefits can be reported near the target optimisation region.

- A shift in hard surge margin has been noted towards higher mass flow rates. This is attributed to exacerbated loading unbalance between main blade and splitter. One possible mitigation strategy encompasses the inclusion of blade loading into the objective function or considering a splitterless design. The findings of this study were presented and will be verified in a future publication.

- An entropy generation based loss study was conducted revealing that the performance benefits were achieved to a great part as a result of a reduction in the entropy produced in the wake region of the impeller trailing edges.

- While the optimisation routine itself is straightforward, relatively simple to implement and does achieve accurate performance predictions, it is possible to further enhance the optimisation procedure and determine the global optimum using a reduced number of costly CFD evaluations through the application of a hybrid approach of a GA and a surrogate model [46]. This will be addressed in a future study.

References

[1] C. Xu, R. Amano, Centrifugal Compressor Design Impacts: Lean and Meridional Shape, Proceedings of the ASME Turbo Expo 5 B (2013).

[2] Newton, P. and Copeland, C.D. and Martinez-Botas, R. and Seiler, M., An Audit of Aerodynamic Loss in a Double Entry Turbine under Full and Partial Admission, International Journal of Heat and Fluid Flow 33 (2012) 70–80.

[3] Hellstrom, F. and Gutmark, E. and Fuchs, L., Large Eddy Simulation of the Unsteady Flow in a Radial Compressor Operating Near Surge, Journal of Turbomachinery 134 (2012).

[4] Palenschat, T. and Newton, P. and Martinez-Botas, R. and Seiler, M. and Mueller, M. and Leweux, J., 3-D Computational Loss Analysis of an Asymmet-

ric Volute Twin-Scroll Turbocharger, in: Proceedings of ASME Turbo Expo 2017: Turbomachinery Technical Conference and Exposition, ASME, 2017.

[5] Olivero, M. and Javed, A. and Van Buijtenen, J.P., Aerodynamic Analysis of a Micro Turbine Centrifugal Compressor, in: Proceedings of ASME Turbo Expo 2010: Power for Land, Sea and Air, ASME, 2010.

[6] Sundstroem, E. and Semlitsch, B. and Mihaescu, M., Assessment of the 3D Flow in a Centrifugal compressor using Steady-State and Unsteady Flow Solvers, SAE Technical Paper 2014-01-2856 (2014).

[7] X. Zheng, Z. Sun, T. Kawakubo, H. Tamaki, Stability improvement of a turbocharger centrifugal compressor by a nonaxisymmetric vaned diffuser, Journal of Turbomachinery 140 (2018).

[8] J. R. Serrano, R. Navarro, L. M. Garcia-Cuevas, L. B. Inhestern, Turbocharger turbine rotor tip leakage loss and mass flow model valid up to extreme off-design conditions with high blade to jet speed ratio, Energy 147 (2018) 1299 – 1310.

[9] M. Padzillah, S. Rajoo, R. Martinez-Botas, A Detailed Comparison on the Influence of Flow Unsteadiness between the Vaned and Vaneless Mixed-Flow Turbocharger Turbine, Journal of Engineering for Gas Turbines and Power 140 (2018).

[10] Wolfgang Sanz and Leitl, Peter A. and Franz Heitmeir, Design and CFD Simulation of a Booster Compressor with Volute, Conference Proceedings (2011) 29–40.

[11] L. Sun, J. Chen, G. Huang, Three-Dimensional Inverse Design of Centrifugal Impeller Blade, in: 51st AIAA/SAE/ASEE Joint Propulsion Conference, AIAA, 2015.

[12] P. He, C. A. Mader, J. R. Martins, K. J. Maki, An aerodynamic design optimization framework using a discrete adjoint approach with OpenFOAM, Computers and Fluids 168 (2018) 285 – 303.

[13] H. Hazby, C. Robinson, M. Casey, D. Rusch, R. Hunziker, Free-form versus ruled inducer design in a transonic centrifugal impeller, Journal of Turbomachinery 140 (2018).

[14] Van den Braembussche, R.A, Numerical Optimization for Advanced Turbomachinery Design, in: Thevenin, D. and Janiga, G. (Ed.), Optimization and Computational Fluid Dynamics, Springer Verlag, Berlin, 2008, pp. 147–188.

[15] K.-K. Ha, S.-H. Kang, An optimization method for centrifugal compressor design using the surrogate management framework, in: SME-JSME-KSME 2011 Joint Fluids Engineering Conference, Fluids Engineering Division, 2011, pp. 679–684.

[16] D. Japikse, Compressor Design and Performance, Concepts ETI, 1996.

[17] Cho, S.-Y. and Ahn, K.-Y. and Lee, Y.-D. and Kim, Y.-C., Optimal Design of a Centrifugal Compressor Impeller Using Evolutionary Algorithms, Mathematical Problems in Engineering 2012 (2012).

[18] L. Bo, G. Chunwei, Numerical Optimization of a Highly Loaded Compressor in SemiClosed Cycles using Neural Networks and Genetic Algorithms, Greenhouse Gases: Science and Technology 6 (2015) 232–250.

[19] Verstraete, T. and Alsalihi, Z. and Van den Braembussche, R.A., Multidisciplinary Optimization of a Radial Compressor for Microgas Turbine Applications, Journal of Turbomachinery 132 (2010) 031004–1– 031004–7.

[20] Kim, J.-H. and Choi, J.-H. and Husain, A. and Kim, K.-Y., Multi-Objective Optimization of a Centrifugal Compressor Impeller Through Evolutionary Algorithms, Proceedings of the Institution of Mechanical Engineers, Part A: Journal of Power and Energy 224 (2010) 711–721.

[21] S. Ibaraki and R. Van den Braembussche and T. Verstraete and Z. Alsalihi and K. Sugimoto and I. Tomita, Aerodynamic Design Optimization of a Centrifugal Compressor Impeller based on an Artificial Neural Network and Genetic Algorithm, in: 11th International Conference on Turbochargers and Turbocharging, Woodhead Publishing, 2014, pp. 65 – 77.

[22] O. Nobuhito, M. Furukawa, K. Yamada, S. Itou, S. Ibaraki, K. Iwakiri, Y. Hayashi, Optimum aerodynamic design of centrifugal compressor impeller using an inverse method based on meridional viscous flow analysis, in: Proceedings of ASME Turbo Expo 2017: Turbomachinery Technical Conference and Exposition, International Gas Turbine Institute, 2017.

[23] C. Vo, M. Aulich, T. Raitor, Metamodel Assisted Aeromechanical Optimization of a Transonic Centrifugal Compressor, 1st TRACE User Conference (2014).

[24] Elfert, M. and Weber, A. and Wittrock, D. and Peters, A. and Voss, C. and Nicke, E., Experimental and Numerical Verification of an Optimization of a Fast Rotating High-Performance Radial Compressor Impeller, Journal of Turbomachinery 139 (2017) 101007–1–101007–9.

[25] U. Siller, C. Voc, E. Nicke, Automated Multidisciplinary Optimization of a Transonic Axial Compressor, 47th AIAA Aerospace Sciences Meeting including the New Horizons Forum and Aerospace Exposition (2009).

[26] T. Raitor, O. Reutter, M. Aulich, E. Nicke, Aerodynamic Design Studies of a Transonic Centrifugal Compressor Impeller Based on Automatic 3D-CFD Optimization (2013).

[27] A. Hehn, M. Mosdzien, D. Grates, P. Jeschke, Aerodynamic optimization of a transonic centrifugal compressor by using arbitrary blade surfaces, Journal of Turbomachinery 140 (2018).

[28] L. Z. Li, X., Y. Lin, Multipoint and Multiobjective Optimization of a Centrifugal Compressor Impeller Based on Genetic Algorithm, Mathematical Problems in Engineering (2017) 1–18.

[29] Z. X. He, X., Performance Improvement of Transonic Centrifugal Compressors by Optimization of Complex Three-Dimensional Features, Journal of Aerospace Engineering 231 (2017) 1–18.

[30] Menter, F.R., Two-Equation Eddy-Viscosity Turbulence Models for Engineering Applications 32 (1994) 1598.

[31] F. Menter, Ten Years of Industrial Experience with the SST Turbulence Model, in: Proceedings of the 4th International Symposium on Turbulence, Heat and Mass Transfer, 2003, pp. 65 – 77.

[32] Ding, MY. and Groth, C. and Kacker, S. and Roberts, D., CFD Analysis of Off-Design Centrifugal Compressor Operation and Performance, 2006 International ANSYS Conference (2006).

[33] Celik, I.B., Procedure for Estimation and Reporting of Discretization Error in CFD Applications, Trans. R. Soc. 130 (2008) 078001–1–4.

[34] SAE-International, SAE J1826 Turbocharger Gas Stand Test Code (1995).

[35] SAE-International, SAE J1723 Supercharger Testing Standard (1995).

[36] ASME, Performance Test Code on Compressors and Exhausters (1997).

[37] ANSYS, ANSYS CFX Users Guide, 2015.

[38] Ding, MY. and Groth, C. and Kacker, S. and Roberts, D., CFD Analysis of Off-Design Centrifugal Compressor Operation and Performance, 2006 International ANSYS Conference (2006).

[39] Vezier, C. and Dollinger, M. and Sorokes, J.M. and Pacheco, J.E., Using Unsteady Analysis To Improve the Steady State CFD Assessment of Minimum Flow in a Radial Compressor Stage, in: Proceedings of ASME Turbo Expo 2013: Turbine Technical Conference and Exposition.

[40] Van den Braembussche, R.A., Optimization of Radial Impeller Geometry, Design and Analysis of High Speed Pumps, Educational Notes RTO-EN-AVT-143, 2006.

[41] Denton, J.D., The 1993 IGTI Scholar Lecture: Loss Mechanisms in Turbomachines, Journal of Turbomachinery 115 (1993) 621–656.

[42] Kock, F. and Herwig, H., Local Entropy Production in Turbulent Shear Flows: A High-Reynolds Number Model with Wall Functions, International Journal of Heat and Mass Transfer 47 (2003) 2205–2215.

[43] Iandoli, C.L. and Sciubba, E., 3-D Numerical Calculation of the Local Entro[y Generation Rates in a Radial Compressor Stage, International Journal of Thermodynamics 8 (2005) 83–94.

[44] Newton, P., Palenschat, T., Martinez-Botas, R.F. and Seiler, M., Entropy Generation Rate in a Mixed Flow Turbine Passage, in: Proceedings of the International Gas Turbine Congress.

[45] Palenschat, T., Newton, P., Martinez-Botas, R.F., Mueller, M. and Leweux, J., 3-D Computational Loss Analysis of an Asymmetric Volute Twin-Scroll Turbocharger, in: ASME Turbo Expo 2017: Turbomachinery Technical Conference and Exposition.

[46] Y. Lian, M.-S. Liou, A. Oyama, An Enhanced Evolutionary Algorithm with a Surrogate Model (2004). `http://citeseerx.ist.psu.edu/viewdoc/download?doi=10.1.1.130.4692&rep=rep1&type=pdf`.